Earth Planet. Sci. Lett. 643 (2024) 118896

Contents lists available at ScienceDirect

Earth and Planetary Science Letters

journal homepage: www.elsevier.com/locate/epsl

Atypical crustal structure of the Makran subduction zone and seismotectonic implications

Chuanhai Yu [a,b], Min Xu [a,b,f,*], Jian Lin [a,b,c,*], Hongfeng Yang [d], Xu Zhao [e], Xin Zeng [e], Enyuan He [a], Fan Zhang [a,b], Zhen Sun [a,b]

[a] Key Laboratory of Ocean and Marginal Sea Geology, South China Sea Institute of Oceanology, Chinese Academy of Sciences, Guangzhou, China
[b] China-Pakistan Joint Research Center on Earth Sciences, CAS-HEC, Islamabad, Pakistan
[c] Department of Ocean Science and Engineering, Southern University of Science and Technology, Shenzhen, China
[d] Earth System Science Programme, Faculty of Science, The Chinese University of Hong Kong, Hong Kong, China
[e] Center of Ocean Expedition, School of Atmospheric Science, Sun Yat-sen University, Zhuhai, China
[f] University of Chinese Academy of Sciences, Beijing, China

ARTICLE INFO

Editor: Dr H Thybo

Keywords:
Makran subduction zone
Crustal structure
Ocean bottom seismometer
Consolidated sediments
Water content
Seismotectonics

ABSTRACT

The Makran subduction zone is atypical due to the thick sediment input and shallow subduction angles, and thus is highly susceptible to megathrust earthquakes. However, the thick sedimentary layers and their underlying crustal structure of the Makran slab are still poorly understood. Here we present a high-resolution crustal velocity model of the Makran subducting slab offshore Pakistan obtained from an active-source wide-angle ocean bottom seismic experiment, revealing fine structure in density and porosity. The results reveal that the incoming sedimentary layer is up to 8.5 km thick with an abrupt gradient change in porosity at 4–5 km depth, indicating a critical depth of compaction and consolidation. The igneous crust is 6–12 km thick with an average subduction dip angle of ∼2°. On either flank of the Little Murray Ridge, divergent crustal structures suggest the plausible existence of distinct tectonic provenances or divergent tectonic evolutionary trajectories for the oceanic crust on each side. The Little Murray Ridge may represent a remnant of the paleo-oceanic boundary, possibly associated with the phenomenon of low-density underplating. The subducting consolidated sediments and uppermost crust with high-water content could significantly influence earthquake rupture mechanisms at both the décollement and igneous basement interfaces. These findings suggest that the décollement and igneous basement interface both have the potential to trigger large earthquakes in the Makran subduction zone.

1. Introduction

Global seismic records of subduction zones indicate a higher likelihood of large earthquakes occurring in subduction zones characterized by low-angle and thick sedimentary coverage (Scholl et al., 2015; Bletery et al., 2016). The Makran subduction zone (MSZ), located offshore Iran and Pakistan in the northwest Indian Ocean and formed by the subduction of the Arabian plate beneath the Eurasian plate (Fig. 1), is considered a global end member subduction zone with shallow dipping slab (2–4°) and thick incoming sediments (>7 km) (Kopp et al., 2000; Smith et al., 2012; Teknik et al., 2019; Motaghi et al., 2020; Priestley et al., 2022). Although the MSZ is relatively seismically inactive compared to other low-angle subduction zones, it has historically generated several destructive earthquakes, primarily offshore Pakistan, including the large earthquake of 1945 M_w 8.1 and subsequent tsunamis which killed more than 4000 people (Byrne et al., 1992; Parvaiz et al., 2022). Recent geodetic plate studies, including GPS (Frohling and Szeliga, 2016; Penney et al., 2017) and InSAR (Lin et al., 2015; Lv et al., 2022), have indicated a strong coupling of the plates, with the potential to generate earthquakes exceeding M_w 8.0. These findings align with results from thermal modeling (Smith et al., 2013; Khaledzadeh and Ghods, 2022) and mechanical modeling (Pajang et al., 2021), which indicate that the Makran coast is one of the regions most severely threatened by earthquakes and tsunamis in the northwestern Indian Ocean.

The Makran Coast lacks sufficient seismic stations, resulting in infrequent instrument-recorded earthquakes despite numerous active faults. The absence of coastal seismic arrays poses a challenge for high-

* Corresponding authors.
E-mail addresses: mxu@scsio.ac.cn (M. Xu), jianlin@scsio.ac.cn (J. Lin).

https://doi.org/10.1016/j.epsl.2024.118896
Received 20 May 2024; Received in revised form 10 July 2024; Accepted 12 July 2024
Available online 23 July 2024

resolution natural seismic imaging of deep structures. Previous research, utilizing land mobile stations, has predominantly focused on the coastal area of Iran in the western Makran region (Fig. 1). Research findings reveal that the sedimentary thickness along the Makran coast can reach 22–28 km (Priestley et al., 2022), and the maximum thickness of the accretionary wedge in the Makran region may even reach 35 km (Haberland et al., 2020), which eliminates the formation of a bathymetric trench. The geological structure offshore Pakistan is much more complicated than that of Iran. Most of the modern seismicity and the significant thrust events historically recorded are concentrated in the areas offshore Pakistan (Fig. 2). Kukowski et al. (2000) revealed a left-lateral strike-slip fault in these areas named Sonne fault (Fig. 1) across the deformation front and the Little Murray Ridge (LMR). The LMR is thought to be a linear basement uplift and is primarily buried beneath sediments, subducting northeastward with the slab (Fig. 2). The property, origin, and age of the presently subducting oceanic lithosphere remain controversial (Edwards et al., 2000) due to the thick sedimentary cover and the absence of identifiable seafloor magnetic anomalies (Fig. 2).

Compared to passive source seismic imaging, active source seismic surveys can usually obtain more detailed velocity structures (Kopp et al., 2000; Haberland et al., 2020). Investigations employing multi-channel seismic (MCS) and sonobuoy surveys in the offshore area of Makran (Fig. 1) reveal the rough velocity structure of the sedimentary layer in the shallow part of the accretion wedge, as well as the morphological characteristics such as gene fold and imbricate thrust faults, contributing to the determination of the deformation front (model distance of 95 km) and the décollement interface locations (Minshull and White,

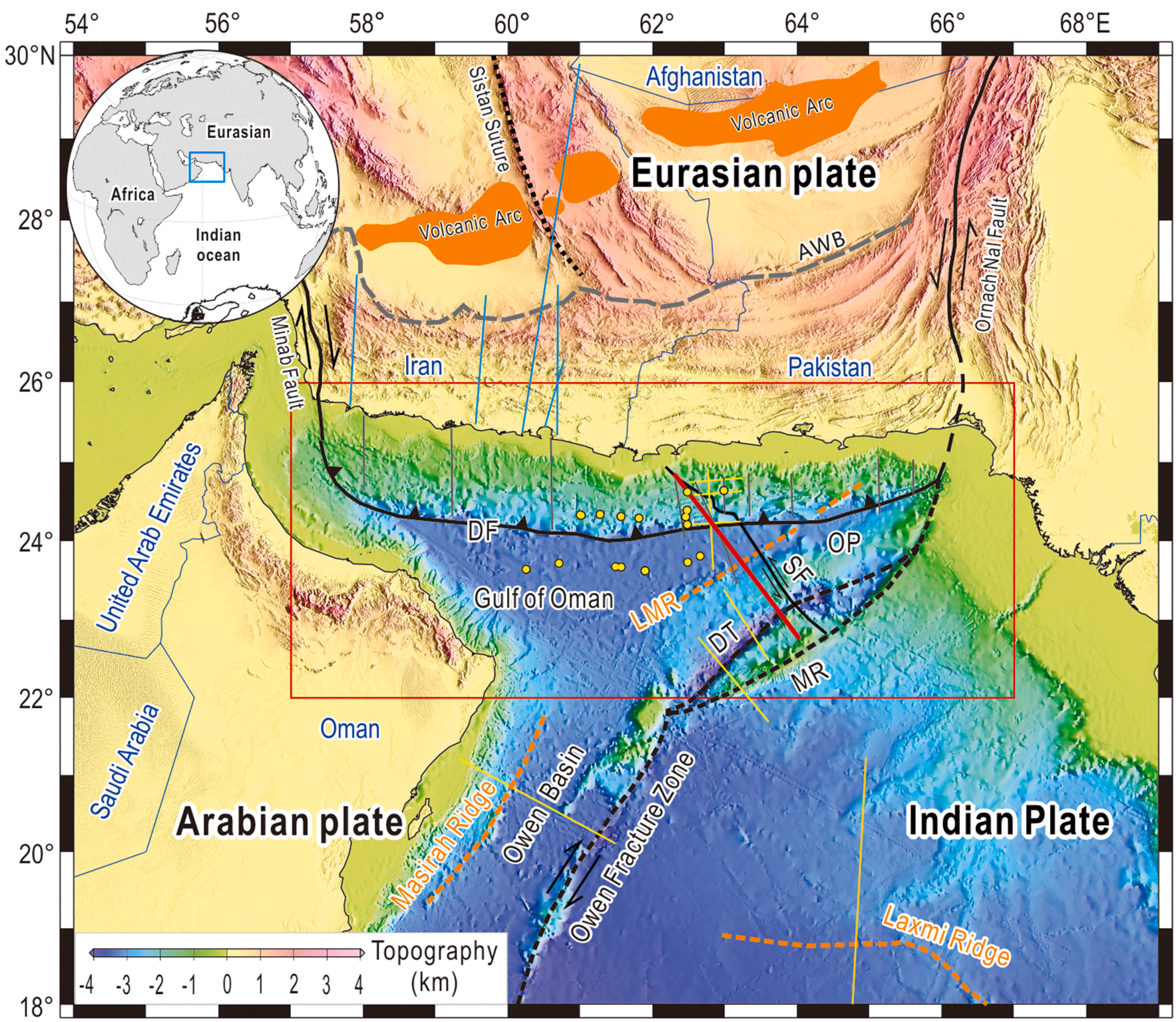

Fig. 1. Topography and tectonic framework of the MSZ. The right-lateral Minab fault is located to the northwest, while the sinistral Ornach Nal fault lies to the northeast. To the south, the Dalrymple Trough and Owen Fracture Zone is the India-Arabia plate boundary (Edwards et al., 2000; Minshull et al., 2015). Thick black lines denote plate boundaries and major faults. Blue lines delineate the trajectory of the deep structure survey line conducted using land mobile stations (Haberland et al., 2020; Motaghi et al., 2020; Priestley et al., 2022), while gray lines depict profiles obtained through multi-channel seismic (MCS) surveys (White and Klitgord, 1976; Minshull and White, 1989; Pajang et al., 2021; Smith et al., 2012). Yellow dots denote the locations of sonobuoy stations (Fowler et al., 1985), and yellow lines represent the profiles derived from ocean bottom hydrophone (OBH) surveys (Barton et al., 1990; Edwards et al., 2000; Kopp et al., 2000; Minshull et al., 2008; Minshull et al., 2015). The red line represents the ocean bottom seismometer (OBS) profile presented in this paper, with the red rectangular box outlining the area depicted in Fig. 2. AWB, Accretionary Wedge Boundary; DF, Deformation Front; DT, Dalrymple Trough; OP, Ormara Plate; LMR, Little Murray Ridge; MR, Murray Ridge; SF, Sonne Fault.

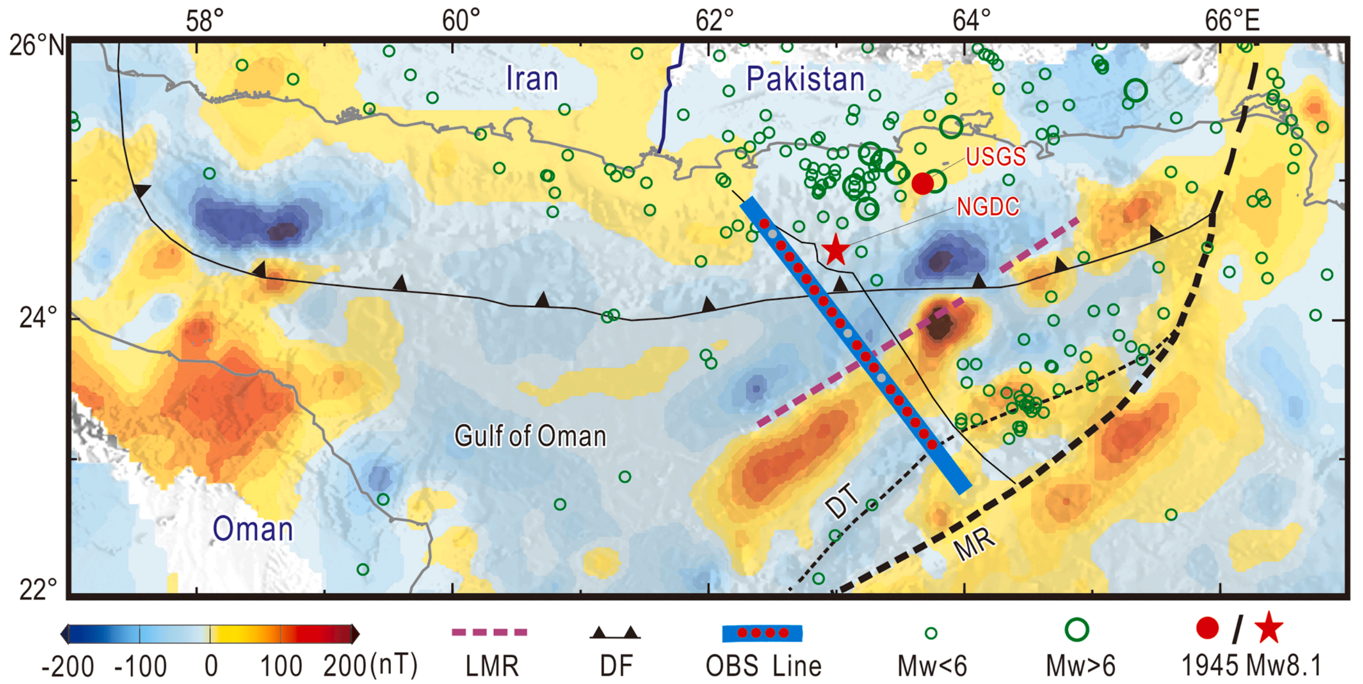

Fig. 2. Marine magnetic anomaly (Meyer et al., 2017) and earthquake distribution superimposed on the topographic grayscale map. Historical earthquake locations are from the United States Geological Survey (USGS). The 1945 M_w 8.1 earthquake locations are from the Global Significant Earthquake Database of the National Geophysical Data Center (NGDC) (red star) and the USGS (red solid circle), respectively. DT, Dalrymple Trough; LMR, Little Murray Ridge; MR, Murray Ridge.

1989; Fowler et al., 1985; Smith et al., 2012). Due to the high acoustic impedance of the thick sedimentary layer, it is difficult to reveal the characteristics of the buried crust offshore Makran with MCS reflection data and sonobuoy data. The only wide-angle reflection/refraction seismic study using the ocean bottom hydrophones (OBHs) of the subducting plate near the deformation front (Fig. 1) shows that the igneous oceanic crust is up to 9 km thick, covered by 3 km thrusting sediments (Kopp et al., 2000). However, OBH investigations across the Murray Ridge (Fig. 1) reveal characteristics indicative of a typical oceanic crust for the subducting plate, featuring an approximate thickness of 6 km adjacent to the north side of Dalrymple Trough (Edwards et al., 2000; Minshull et al., 2015). The observed crustal thickness of the subducting plate is comparable to that observed onshore in the Iranian region (Fig. 1), as determined through receiver function and surface wave analysis (Motaghi et al., 2020; Priestley et al., 2022). The limited wide-angle reflection/refraction seismic investigation along the whole subducting plate makes the characteristics of crustal structure and properties of MSZ enigmatic.

It has been shown that the properties of incoming oceanic lithosphere, such as age, dip, structure, sedimentary thickness, and hydration status, can control the tectonic geometry, plate coupling, and earthquake potential of subduction zones (e.g., Han et al., 2017; Frohling and Szeliga, 2016; Olsen et al., 2020). The crustal structure of the subducting oceanic lithosphere contains valuable information about its morphology and tectonic evolution (Contreras-Reyes et al., 2008; Allen et al., 2022). Accurate measurements of crustal velocity structure and interface information are the key to studying the modification of the oceanic plate and the tectonic framework of subduction zones, and hence the plate coupling and seismogenic structure of the MSZ (Khaledzadeh and Ghods, 2022; Yang et al., 2022).

In this study, we present high-resolution crustal velocity structure and interface geometry of subducting plate offshore Pakistan in the MSZ by the recently acquired wide-angle OBS data and systematically assess the crustal properties from the Dalrymple Trough to the north of the deformation front. Furthermore, we discuss sediments consolidation, tectonic framework, plate hydration, and seismicity, which may provide valuable references for future assessments of seismogenic potential and tsunami hazards in the MSZ.

2. Data processing and velocity modeling

2.1. Data acquisition

In February 2018, the R/V ShiYan 3 of the South China Sea Institute of Oceanology conducted the first joint China-Pakistan Northern Indian Ocean scientific cruise. During the cruise, a ~280 km long wide-angle seismic profile was acquired (Fig. 1), coinciding with multibeam data (Fig. S1), gravity, and a 24-channel seismic reflection profile (Fig. S2) along the NW-SE profile. Twenty-one four-component OBSs were deployed with a spacing of ~11 km, crossing the Dalrymple Trough, LMR, and the deformation front from the Murray Ridge to the Makran accretionary wedge, which is the latest active-source OBS seismic profile spanning the Arabian Plate, the Eurasian Plate, and the northern side of the Indian Plate. Twenty OBSs were successfully recovered, but two could not provide valuable data. The seismic source was an array of four BOLT airguns with a total volume of 6000 cubic inches. The shot interval was set to 90 s to meet the working pressure of ~2000 psi (138 Bar), leading to ~250 m shot spacing on average, and a total of 1096 shots were fired from northwest to southeast. Each OBS was equipped with a hydrophone and a three-component seismometer. The majority of OBS instruments recorded data at a sampling rate of 100 Hz, with exceptions noted for OBS10 (250 Hz), OBS16 (250 Hz), and OBS20 (50 Hz), as delineated in Table S1. Generally, vertical seismometer records demonstrated superior signal-to-noise ratios, although data from the hydrophone were employed whenever practicable.

2.2. Data processing

The raw OBS data were converted and split into four single shot records (three- geophones and one hydrophone) as the receiver gathers SEG-Y format after correcting the clock-drift of shot records and relocating the positions of instruments. The relocation of OBS on the seafloor based on direct arriving water-wave data and precise shot locations determined by GPS, aiming to correct for possible instrument drift during deployment. Band-pass filter tests show that the seismic phases with a high signal-to-noise ratio can be acquired in the 3–15 Hz range. We manually picked 6232 refraction and 6968 reflection arrivals (Table S2). Eight types of *P*-wave arrivals were identified (Fig. 3), including three refraction phases within the sedimentary succession (*Ps*), the crust (*Pg*), and the uppermost mantle (*Pn*), and five reflection phases from the interface of the sedimentary unconformity (*Ps1P, Ps2P*), the igneous basement (*PbP*), the mid-crustal (*PcP*), and the Moho discontinuity (*PmP*). The traveltime picking errors were assigned as 30 ms in near offsets and 50–80 ms in far offset arrivals during model inversion.

2.3. Velocity modeling

We used the joint seismic refraction and reflection traveltime inversion method (Tomo2D) of Korenaga et al. (2000) to build the *P*-wave velocity model and ray tracing. The Tomo2D code can solve the forward problem based on the reference model and manually picked arrivals, and invert for the velocity field and the interface depth of reflection. We implemented a 'top to bottom' approach using a simple layered initial model, in line with the methodologies outlined in Shulgin et al. (2013). The tomography model is defined on a regular two-dimensional grid with a constant spacing of 0.25 km in both the vertical and horizontal dimensions. The starting model used for inversion consists of 5 layers: seawater, sedimentary succession, upper crust, lower crust, and uppermost mantle. Initial seafloor depth came from the multibeam bathymetry data (Fig. S1). The initial basement was constrained by multi-channel seismic data (Fig. S2), *PbP* reflection arrivals, and previous geophysical results (e.g., Kopp et al., 2000; Smith et al., 2012). During inversion, we first verified consistency by inverting near offset refracted phases, followed by fixing the upper model section and iteratively inverting for subsequent layers' velocity and reflector geometry, ultimately fixing the entire crustal structure before inverting for upper mantle velocity (Shulgin et al., 2011; Planert et al., 2010). We used the values of horizontal correlation lengths varying from 2 km at the seafloor to 5 km at the bottom of the model, and vertical correlation lengths increased from 1 km at the seafloor to 2 km at the bottom of the model. The depth kernel weighting parameter was set to 1 to favor equally weighted perturbations of velocity and interface depth (Korenaga et al., 2000). The velocity and depth smoothing values were set to 80 and 5, respectively. Each layer of the model underwent approximately 5–7 iterations to achieve optimal fitting with seismic phases.

The chi-square (χ^2) value obtained for the best-fitting model (Fig. 4a) is 1.07. The detailed root-mean-square (RMS) and χ^2 values are shown in Table S2. The fit between observed and calculated arrivals and the corresponding ray path is shown in Fig. 3. The OBS data provides the velocity model with excellent ray coverage. A measure of ray coverage density of the best-fitting model was quantified by calculating the derivative weight sum (DWS), as shown in Fig. 4b.

2.4. Resolution tests

We conducted tests to assess the resolution of our intermediate and final models. Initially, we used a forward ray shooting method to compute travel times for first arrival and reflected phases. Fig 3 illustrates the comparison between seismic sections and calculated travel times at OBS10 and OBS18 stations, showing good agreement between the predicted travel times and recorded seismic sections for refracted and reflected phases. We also performed a series of checkerboard tests on the best-fitting model results, including the scales of 15 km (horizontal) × 5 km (vertical), 10 km × 4 km, 8 km × 4 km, and 6 km × 4 km in both sediments and igneous crust, with a perturbation value of ±5% (Fig. S3). Good recovery of velocity pattern was obtained at depths shallower than 15 km, except for the northern region of the accretionary prism (model distances of 20–60 km), where the recovery below 10 km depth was poor (Fig. S3) due to limited ray coverage. Likewise, resolution testing confirms that the igneous crustal structure beneath the sedimentary layer maintains the capacity to distinguish anomalous bodies measuring 8 km × 4 km at a depth of 20 km (model distances of 60–250 km).

3. Results

3.1. Sedimentary layer

The tomographic velocity model and DWS (Fig. 4) reveal a relatively high ray density coverage within the model distance of 30–240 km, with the seismic waves sampling to a maximum depth of 23 km. Notably, the characteristics of thicknesses, velocities, and structures on the north and south sides of the LMR differ significantly. The sedimentary cover atop the subducting plate gradually thickens from south to north, with sedimentary layers reaching a maximum thickness exceeding 13 km. In the south of the LMR, the subducting plate is covered by a thin sedimentary layer (1.5–2.2 km) exhibiting seismic velocities ranging from 1.9 to 2.7 km/s. Moving northward from the LMR, the sedimentary thickness exceeds 4.5 km, while near the deformation front of the subduction plate, it measures approximately 8.5 km.

In regions characterized by thick sediments, two reflective interfaces have been identified within the sedimentary layer. From the LMR to the vicinity of the deformation front, an apparent sedimentary unconformity interface is identified in both the OBS velocity model (Fig. 4) and the MCS data (Fig. S2), with a sedimentary thickness ranging from 0.9 to 1.8 km above the interface. Below this unconformity interface, another distinct reflection interface is identified, roughly aligning with a velocity contour line of 4.0 km/s, extending from a location 38 km south of the deformation front to 73 km north of it (model distance of 22–132 km). The sedimentary thickness above this interface ranges from 4 to 5 km, with the velocity increasing rapidly from 2.0 km/s to 4.0 km/s from the seafloor to this interface. The velocity gradient in the shallow part is as high as 0.7 (km/s)/km, rapidly decreasing to 0.1 (km/s)/km at depths below this interface, where the sediments velocity stabilizes at 4–4.5 km/s.

3.2. Igneous crust

In the surveyed area, no evidence of continental crustal structure was discerned, nor were seismic reflections indicative of a décollement observed along the OBS profile. However, the continuous presence of basement and Moho interfaces of the subducting plate was readily identifiable. The subduction angle, determined using the basement dip, is approximately 2° in the region north of the LMR (model distance of 50–120 km), while the basement dip of the abyssal plain in the region south of the LMR is approximately 1° (160–200 km). The section where the profile traverses the linear LMR exhibits no exposed basement outcrops, but has distinct features indicative of crustal thickening. Notably, the basement dip in the northern vicinity of the LMR (120–160 km) is as significant as 5–8°

The crustal thickness of the subduction plate varies from 6 to 12 km, with the area north of the LMR exhibiting greater thickness compared to the relatively thinner southern region. The velocity values for the uppermost and lower portions of the igneous crust are in the range of 4.2–4.8 km/s and 7.5–7.8 km/s, respectively. While the velocity model provides limited insight into mantle structure, data pertaining to the uppermost mantle suggests velocities ranging from 7.8 to 8.3 km/s. In the area north of the LMR, the crustal thickness measures 8–9 km, featuring a distinct upper-lower crustal interface. The upper crust is approximately 5 km thick, while the lower crust is 3 to 4 km thick. Notably, the velocity gradient in the upper crust is higher than that in the lower crust. Conversely, in the area south of the LMR, the crust

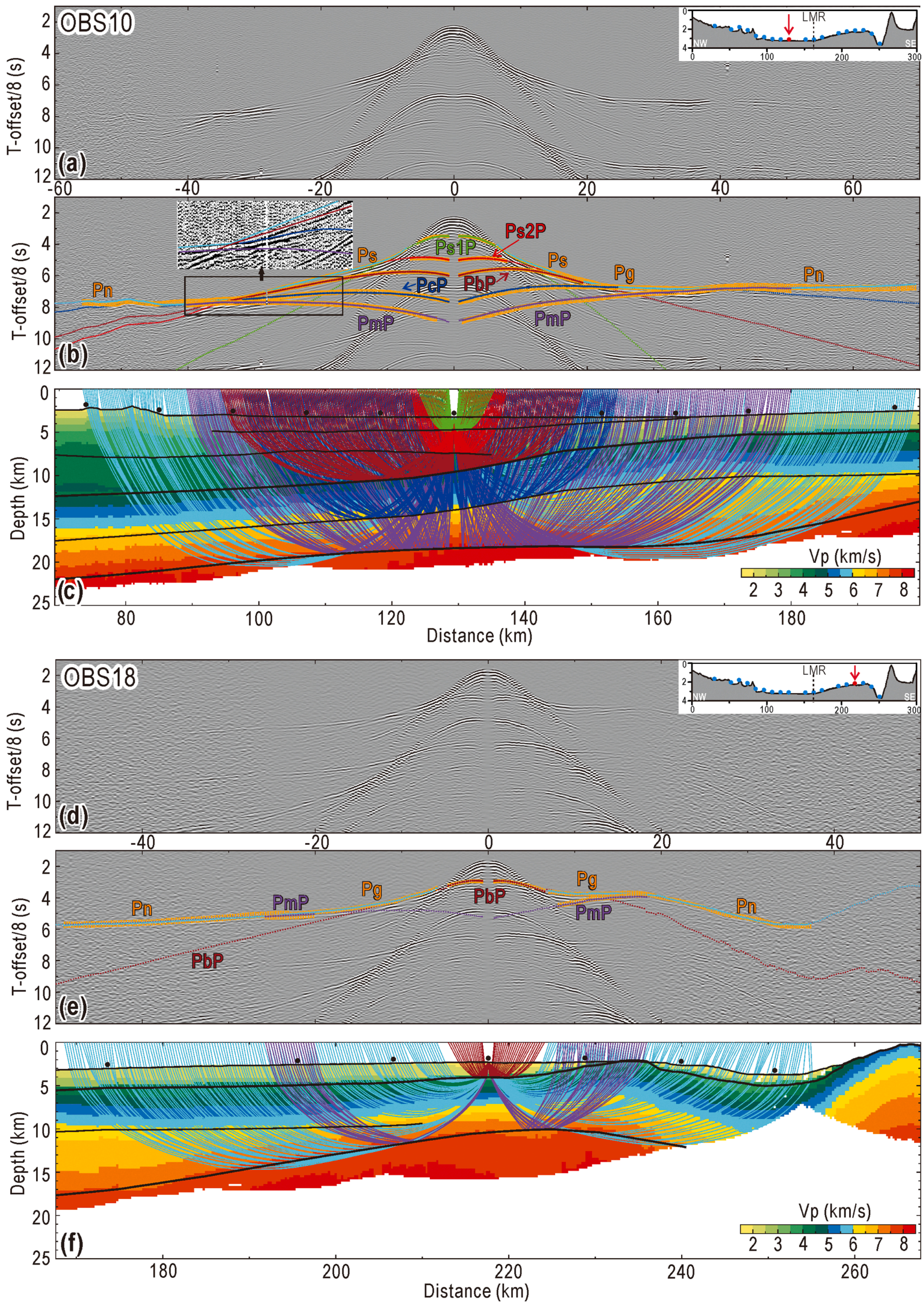

Fig. 3. Examples of vertical component data from the seismic record of OBS10 and OBS18. (a), (d) Seismograms with reduction velocity of 8.0 km/s; (b), (e) Comparison of picked (with error bars) and calculated arrivals. Picked arrival times for refraction phases (orange) and reflection phases (orange) are plotted with calculated arrival times based on the final velocity model for refraction phases (cyan) and reflection phases (*Ps1P*: green; *Ps2P*: red; *PbP*: brown; *PcP*: blue; *PmP*: purple). *Ps*: refraction in the sedimentary succession; *Pg*: crust refraction; *Pn*: uppermost mantle refraction; *Ps1P*: first intra-sediment reflection; *Ps2P*: second intra-sediment reflection; *PbP*: basement reflection; *PcP*: mid-crustal reflection; *PmP*: Moho reflection. (c), (f) Corresponding ray path is plotted and superimposed on the final velocity model. The seismic data are bandpass filtered to 3–15 Hz.

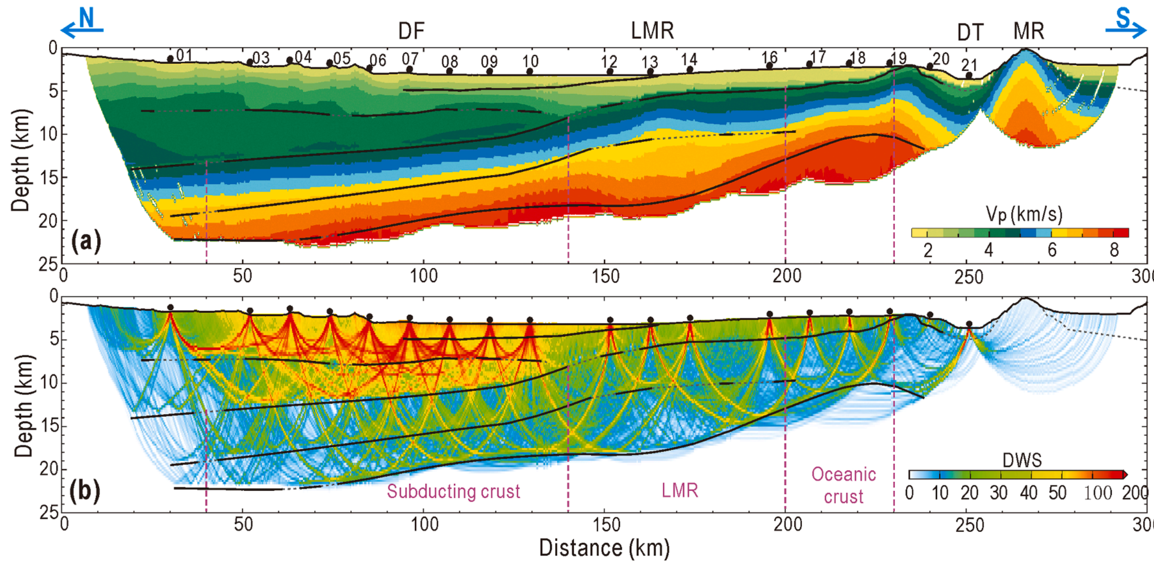

Fig. 4. (a) Final velocity model with all reflective interfaces indicated by dotted lines. Interfaces are highlighted in thick black solid lines where constrained by reflective phases. (b) The corresponding DWS. The purple dashed lines separate the crustal segments with good ray coverage in Fig. 6. DF, Deformation Front; DT, Dalrymple Trough; LMR, Little Murray Ridge; MR, Murray Ridge.

gradually thins to 6 km, with few continuous intra-crustal reflections observed (Figs. 3 and 4). An uplifted high-velocity zone is identified in the region north of Dalrymple Trough, outcropping to the seafloor between OBS19 and OBS20 stations. The crustal thickness of the LMR is up to 12 km, characterized by crustal thickening, with an uplifted high-velocity zone present in the upper crust. Additionally, a relatively low-velocity anomaly zone is observed at the bottom of the lower crust above the Moho interface with a seismic velocity of approximately 7.5 km/s.

4. Discussion

4.1. Décollement and consolidated sediments

Our velocity model highlights that the thickness of the incoming sediments within the MSZ extends to 8.5 km, slightly higher than the 7.5 km identified by the MCS data (Smith et al., 2012). Within our OBS model, the sedimentary unconformity, delineated by the first shallow reflection interface within the sedimentary layers, partitions the incoming sediments near the deformation front into two distinct sequences: an upper sequence measuring ~2.7 km thick, consisting of slop-shelf sands and hemipelagic sediments, and a lower sequence with a thickness of ~5.8 km, comprising Himalayan turbidites. These findings align with the results reported by previous MCS data (Smith et al., 2012). Minshull and White (1989) proposed that variations in sediments sources and mechanical properties in the accretion wedge could develop the unconformity into a décollement interface. However, the décollement inferred from the geometry of thrust faults and the undeformed subducting sediments lie below the unconformity, approximately 5 km below the seafloor (Smith et al., 2012). Grando and McClay (2007) further suggested that the décollement may reside within an overpressured shale layer in the lower Himalayan turbidites sequence. The accretion or detachment of sedimentary layers and the seismogenic properties are closely related to the consolidation status of sediments within the accretion wedge and incoming sediments (Smith et al., 2014; Han et al., 2017). To assess the difference of compaction levels in our model, we categorize the sediments velocity data constrained by good ray coverage (model distance of 20–220 km) into three categories (Fig. 5): the accretion wedge (20–95 km), thick incoming sediments (TIS) (95–140 km), and abyssal plain (140–220 km). Thus, representing accreted sediments influenced by lateral underthrust and vertical loading forces, normally compacted thick sediments unaffected by subduction or accretion, and pelagic sediments with minimal thickness, respectively.

Compared to other subduction zones with thick sedimentary cover (Fig. 5a), the sediments velocity structure within the upper 4.5 km of our model resembles that of Cascadia and Alaska, slightly lower than that of Sumatra. However, our model reveals a notable change in velocity gradient beneath the second shallow reflection interface within the sedimentary layers, occurring at ~4.5 km depth, which differs from patterns observed in other thick-sediments-covered subduction zones. Above this interface, velocity experiences a rapid increase with depth, exhibiting minimal change thereafter. This trend is in agreement with laboratory measurements demonstrating velocity variations with effective stress in both dry and saturated rocks (Khaksar and Griffiths, 2000). We interpret this phenomenon as the gradual compaction, dehydration, and consolidation of shallow sediments with high porosity as burial depth increases. At ~4.5 km depth, sedimentary rock reaches a critical threshold, resulting in a qualitative change in rock rigidity. The reflection interface could potentially signify the boundary of this compacted consolidation. Consequently, the sedimentary rock below this interface exhibits increased stress-bearing capacity, leading to a reduction in velocity variation with depth.

To examine the porosity structure, we utilized global empirical relationships to convert the seismic velocity into porosity (see Text S1). Both velocity-depth and porosity-depth data reveal a consistent pattern between the accretion wedge and TIS, particularly in the comparable gradient change occurring at a depth of ~4.5 km (Fig. 5). This suggests that, in the Makran region, the predominant influence on profound sediments dehydration and porosity reduction stems from the loading force exerted by thick sediments, rather than thrust stress. Referring to the décollement location revealed by Smith et al. (2012), it is located below the sediments consolidation interface. This suggests that incoming sediments undergo significant dewatering and consolidation under compaction at a depth of ~4.5 km prior to subduction. Consequently, the velocity (4–5 km/s) and porosity (below 10%) of sediments below 4.5 km remain stable within a particular range and change minimally with the depth during subduction. This is supported by thermal modeling results (Smith et al., 2013) and MCS data (Smith et al., 2014), which suggest that fluid expulsion primarily occurs in the upper 4 km, while deeper sediments consolidate within accretion wedge of Makran. Velde (1996) also found that the sediments porosity decreased

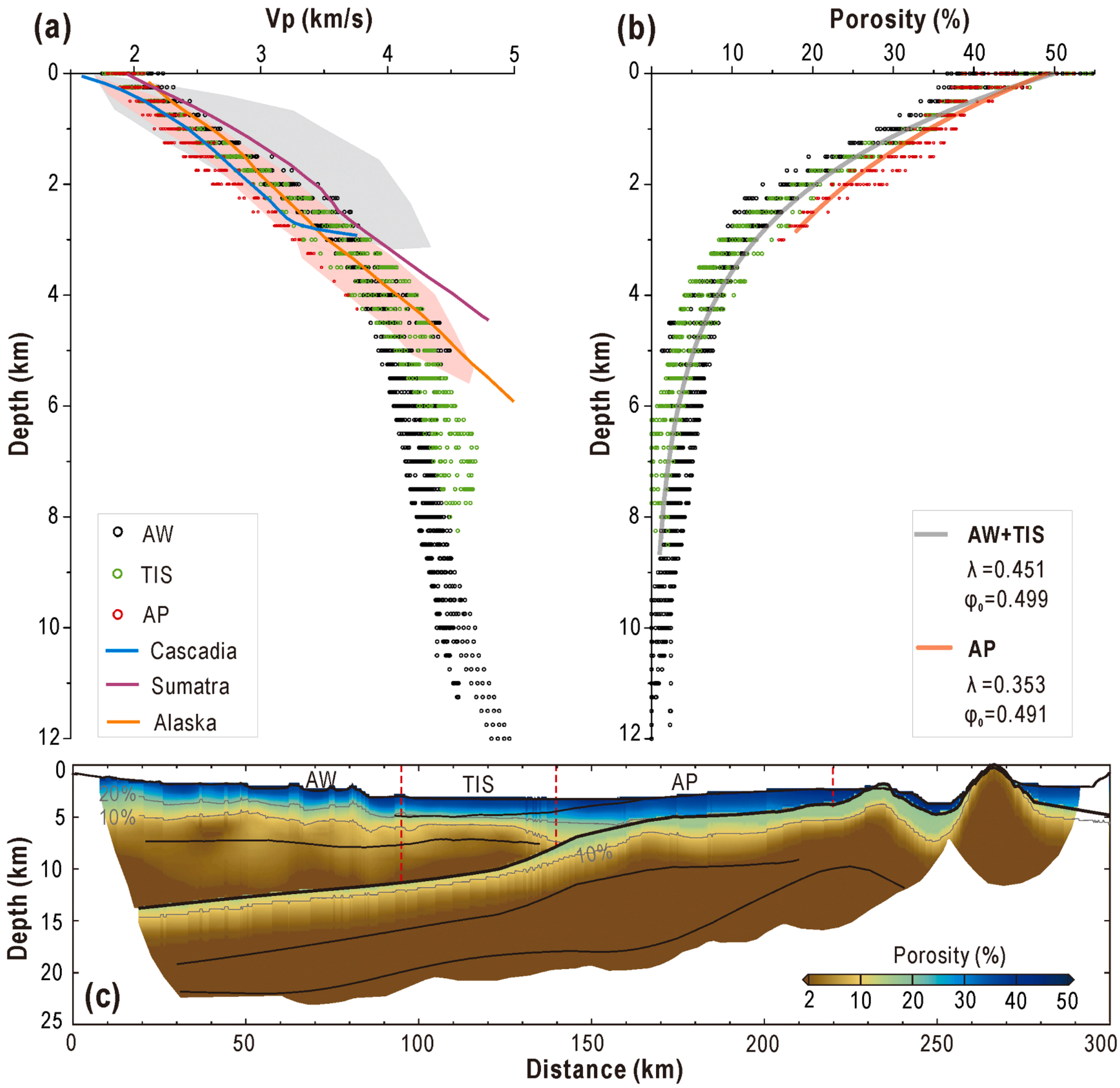

Fig. 5. (a) Velocity-depth data of sediments below the seafloor. Colored curves are sediments velocity profiles from Cascadia, Sumatra, and Alaska (Han et al., 2017). The gray shaded area is the velocity-depth data envelope of the accretion wedge in Makran based on the MCS results of Minshull and White (1989), and the pink shaded area is the corresponding envelope of the TIS area (classified as abyssal plain in their categories); (b) Porosity-depth data converted from the velocity model (see Text S1). Data point colors are the same as for (a) classification. The black curve is Athy's relationship curve fitted to the area of the accretion wedge and TIS. Due to compaction diagenesis, the porosity-depth gradient changes significantly in the shallow part and varies little within the deep region. Only the data above 8 km depth were fitted to obtain the compaction parameters of thick sediments. The red curve is Athy's relationship curve fitted to the abyssal plain. Athy's relationship: $\varphi = \varphi_0 * e^{-\lambda * z}$, where φ is the porosity, φ_0 is the porosity of material at the surface, λ is the compaction constant, and z is the burial depth; (c) Porosity distribution of sediments and oceanic crust along the profile. AW, accretion wedge; TIS, thick incoming sediments; AP, the abyssal plain.

rapidly from 40% to 10% in the depth range of 0.5–4 km through statistical analysis of porosity data from boreholes and deep wells. If this is the case, the unreflective décollement may be interpreted as low-porosity subducted sediments consolidating into rocks prior to subduction, resulting in little velocity contrast with the overlying consolidated sediments. Therefore, no apparent high amplitude or negative polarity reflectors are evident in MCS data (Smith et al., 2012) and our OBS velocity model.

Our model offers a significantly larger dataset, encompassing more tectonic units and greater depths than previous studies employing sonobuoy, MCS, and OBH data in the Makran region (Fowler et al., 1985; Minshull and White, (1989); Kopp et al., 2000). Their velocity-depth distribution from Fowler et al. (1985) and Minshull and White (1989) aligns with our results in the TIS area, yet exhibiting slightly higher values within the upper 3 km of the accretion wedge (Fig. 5). They interpreted the velocity-depth discrepancy between the accretion wedge and TIS as indicative of lateral forces within the accretion wedge, resulting in greater sediments consolidation compared to the TIS area. Similar distinctions are observed between the accretion wedge and the abyssal plain in our model. The sediments in the abyssal plain exhibits slightly steeper porosity-depth gradients compared to the accreted sediments, suggesting that the latter, subject to horizontal thrust compression, may undergo slightly more effectively dewatering than the abyssal plain sediments. Furthermore, variations in sediments sources between the shallow accretion wedge (comprising hemipelagic sediments and slop-shelf sands) and abyssal plain (comprising pelagic sediments and Himalayan turbidites) also affect sediments compaction characteristics. By fitting porosity-depth data of sediments with Athy's relationship, we derived the compaction constants for the accretion wedge and abyssal plain, depicted in Fig. 5b, revealing that the accreted sediments are more prone to compaction compared to those in the abyssal plain. Specifically, the compaction constant for the accretion wedge (0.451) in Makran aligns closely with the value reported for Cascadia (0.4601) (Han et al., 2017) but notably smaller than that obtained by Minshull and White (1989) in Makran (0.7692).

4.2. The role of LMR in controlling crustal structure

The LMR roughly separates the crustal structure and properties of the subducting plate. In the northern region, characterized by thick sedimentation, a relatively steep dip of the basement, and a thick crust, our observations align with those of Kopp et al. (2000). Conversely, the southern region exhibits thinner sedimentation, a shallower dip angle of the basement, and a thinner crust, consistent with the findings of Edwards et al. (2008) and Minshull et al. (2015). The velocity characteristics are delineated into three segments (Fig. 4): the subducting oceanic crust to the north (model distance of 40–140 km), the LMR (140–200 km), and the oceanic crust to the south (200–230 km). One dimensional (1D) analysis of the velocity structure reveals significant differences in velocity gradient between the northern and southern sides of the LMR (Fig. 6). The velocity gradient value in the crust north of the LMR is smaller than that in the crust south of the LMR. The velocity structure of the LMR (Fig. 6) is similar to that of the northern subducting oceanic crust but exhibits thicker crust and lower velocity values, obviously different from the southern oceanic crust. In the region north of the LMR, a continuous intra-crustal reflector is observed, a feature also noted in the eastern Indian Ocean by Altenbernd et al. (2020; 2022), who suggested it may represent a unique characteristic of the Indian Ocean crust. The 1D velocity analysis further highlights significant differences in crustal structure between the Makran region and the Pacific

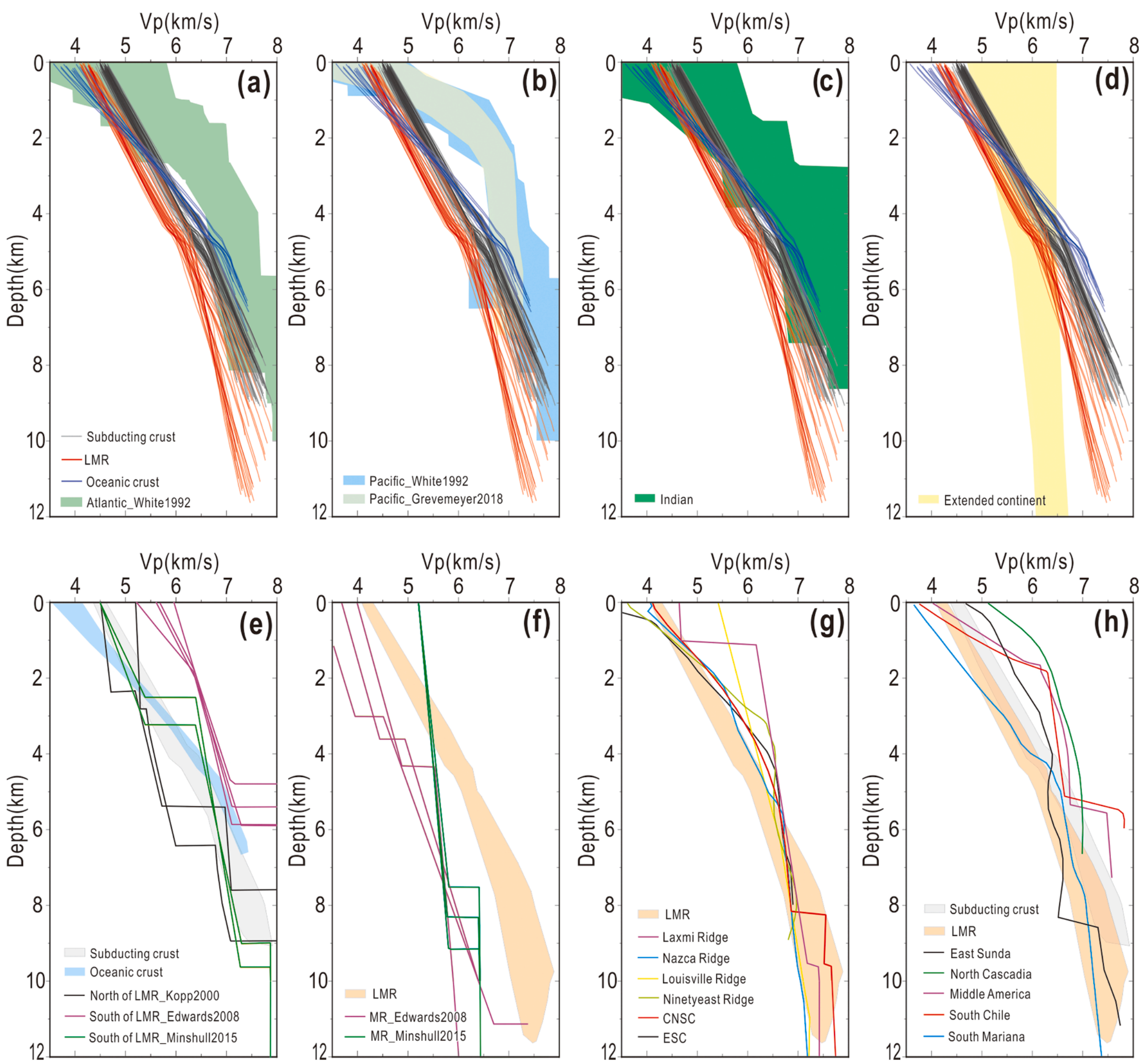

Fig. 6. Compilation of crustal velocity profiles of Makran. (a-d) The gray, red, and blue curves represent velocity-depth structures from the top of the crust in three segments covering model distance of 40–140 km (subducting oceanic crust), 140–200 km (LMR), and 200–230 km (oceanic crust) of the MSZ, extracted at 2 km intervals along the section. These 1D velocity-depth curves are superimposed on the color envelopes depicting (a) typical velocities for the Atlantic oceanic crust (0–170 Ma) (White et al., 1992), (b) typical velocities for the Pacific oceanic crust (0.2–140 Ma) (White et al., 1992; Grevemeyer et al., 2018), (c) velocities for the Indian oceanic crust (Grevemeyer et al., 2001; Zhao et al., 2013; Niu et al., 2015; Altenbernd et al. 2020; 2022; Contreras-Reyes et al., 2023), and (d) the extended continental crust (Christensen and Mooney, 1995). (e-h) The gray, orange and cyan envelopes represent velocity ranges for model distances 40–140 km (subducting oceanic crust), 140–200 km (LMR) and 200–230 km (oceanic crust), respectively. These envelopes are superimposed by the color curves indicating (e) velocities for the north of LMR (Kopp et al., 2000), (f) velocities for the south of LMR and Murray Ridge (Edwards et al., 2008; Minshull et al., 2015), (g) velocities for the Laxmi Ridge (Minshull et al., 2008), Nazca Ridge (Contreras-Reyes et al., 2022), Louisville Ridge (Contreras-Reyes et al., 2010), Ninetyeast ridge (Grevemeyer et al., 2001), Cocos Nazca Spreading center (CNSC) (Van Avendonk et al., 2011), and Emperor seamount chain (ESC) (Watts et al., 2021), and (h) velocities for East Sunda (Planert et al., 2010), North Cascadia (Canales et al., 2017), Middle America (Ivandic et al., 2008), South Chile (Contreras-Reyes et al., 2008), and South Mariana (He et al., 2023), respectively.

Ocean or Atlantic Ocean (Fig. 6a-c). In the area south of the LMR, no clear intra-crustal reflection phase is evident, a finding somewhat divergent from Edwards et al. (2008), who reported a distinct intra-crustal interface on the northern side of Dalrymple Trough.

In comparison with the existing velocity structures of the Makran region, the velocity values for the area north of the LMR (gray envelope in Fig. 7e) are slightly higher overall than those reported by Kopp et al. (2000) for the region north of the deformation front, yet both models exhibit similar crustal thickness. Conversely, for the area south of the LMR (cyan envelope in Fig. 7e), the velocity is slightly higher than the results of Minshull et al. (2015) but lower than those reported by Edwards et al. (2008), while the crustal thickness resembles the findings of Edwards et al. (2008). Comparatively, the crustal velocity of the LMR, especially in the lower crust (Fig. 7d and 7f), demonstrates significantly higher values than that of the Murray Ridge, located north of the LMR and considered a thinned continental crust (Minshull et al., 2015; Edwards et al., 2008). Meanwhile, the 1D velocity structure of the LMR resembles the Laxmi Ridge (Fig. 7g), which coincides with a gravity low and thick crust covered by up to 4 km of sediments in the western margin of India (Fig. 1) and is deemed to have local magma underplating (Minshull et al., 2008). Moreover, the crustal structure and thickness characteristics of the LMR also resemble those of ridge or hotspot track formations related to magmatic intrusions near the other subduction zones, such as the Nazca Ridge in the Peru-Chile subduction zone, Louisville ridge in the Tonga-Kermadec subduction zone, Cocos Nazca Spreading center in the Middle America subduction zone, Ninety East Ridge, and Emperor seamount chain (Fig. 7g). Van Avendonk et al. (2011) suggested that this unusual crustal structure might be related to the early igneous processes. However, similar low velocity and large crustal thickness characteristics can also result from serpentinization associated with subduction plate bending faults, as observed in the eastern part of Sunda and southern Mariana (Fig. 7h). Nonetheless, given the presence of thick low-permeability sediments, significant crustal thickening, and the linear arrangement feature of the LMR, we suggest that the crustal structural characteristics of the LMR are more likely attributable to deep magmatic activity. Seismic velocity is converted to saturated bulk density using empirical relationships (see Text S2) with the constraint of gravity data collected during the cruise, as shown in Fig. 8. The analysis reveals the necessity for a low-density block to adequately fit the measured gravity data well below the LMR. Similar to ridge structures with magmatic intrusions, as shown in Fig. 7g, we speculate that low-density underplating may also exist in the deeper part of the LMR.

There are two main hypotheses regarding the evolution of the subducting oceanic crust in Makran. The first hypothesis suggests that the plate boundary has been located along the Owen Fracture Zone since the northward movement of India at 90 Ma, and the subducting oceanic crust in Makran is the remnant of the Neo-Tethys and formed during the Late Jurassic-Early Cretaceous period (Whitmarsh, 1979). The second hypothesis suggests that the plate boundary was initially located along the Oman continental margin and subsequently shifted to the present-day Owen Fracture Zone, resulting in the subducting oceanic crust in Makran, a collage of Neo-Tethys and East Somali Basin, which formed during the period of Paleocene-Eocene or Late Cretaceous (Rodriguez et al., 2020). Seismic profile across the southeast Oman continental margin have indicated the presence of strike-slip motion along the margin (Barton et al., 1990), which lends support to the second hypothesis. Additionally, the absence of an oceanic magnetic stripe, typically formed during the magnetostatic period, along with cooling models constrained by heat-flow data, suggests a Late Cretaceous age for the subducting oceanic crust (Hutchison et al., 1981; Edwards et al., 2000). Our findings suggest that the subduction plates of Makran may comprise oceanic crust with varying characteristics. Whitmarsh (1979) proposed that the LMR may be connected to the Masirah ridge in the Owen Basin (Fig. 1), which are typical of large volcanic seamounts (Barton et al., 1990). Linear arrangement of these volcanic reliefs in the Indian Ocean often indicates the presence of fossil ocean-ocean transitions (Rodriguez et al., 2020). If the linearly arranged LMR represents the boundary between different tectonic domains, it likely denotes the paleo-ocean boundary between the Neo-Tethys and East Somali Basin. However, it is also possible that linear ridges in the North Indian Ocean, including the LMR, may be related to multiple magmatic events associated with the Deccan Traps considering the similarity in velocity structure between the LMR and the ridges affected by hotspots (Fig. 7g). Crustal thickness differences between the south and north of the LMR may also result from magmatic activity in the south, potentially induced

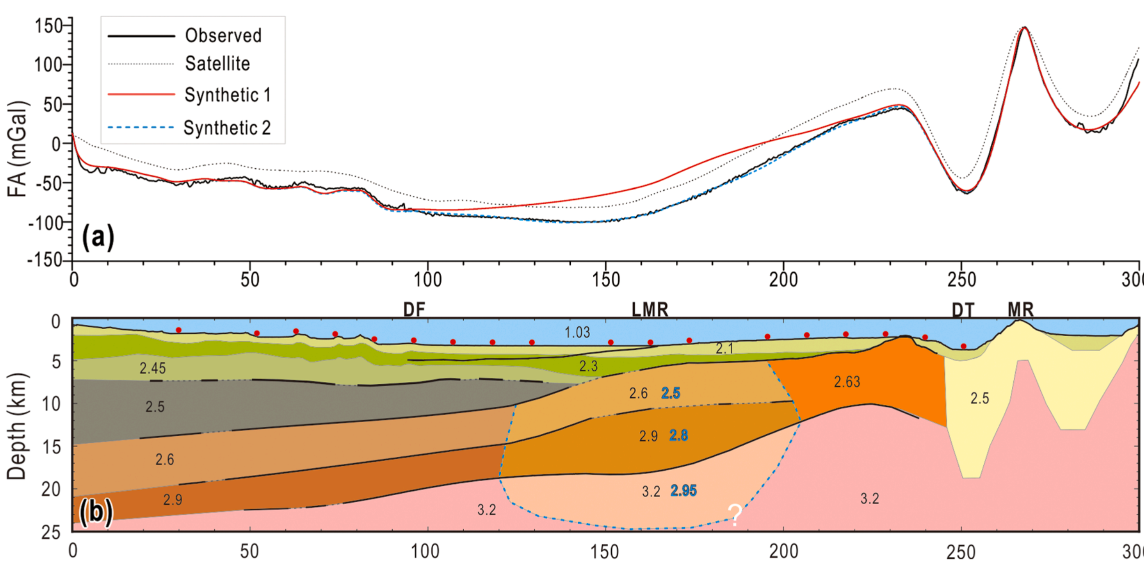

Fig. 7. (a) Dotted and solid black lines represent the free air gravity anomaly extracted from the global satellite gravity model (Sandwell et al., 2014) and collected during this cruise, respectively. The red curve (synthetic 1) depicts the synthetic gravity anomaly calculated from the velocity-derived density model. The dashed blue curve (synthetic 2) depicts the best-fitting synthetic gravity anomaly calculated from the adjusted and preferred density model. (b) The density-depth model derived from our velocity structure and interface geometry. The black numbers are the average density values of each block, corresponding to the gravity anomaly of synthetic 1. According to the position of the intra-crustal interface in the velocity model and the shape of the deep structure, we effectively fit the observed gravity anomaly data by reducing the density value below the LMR. The dashed blue curve envelopes the area where the density value is adjusted. The blue numbers denote the adjusted density value corresponding to the gravity anomaly of synthetic 2.

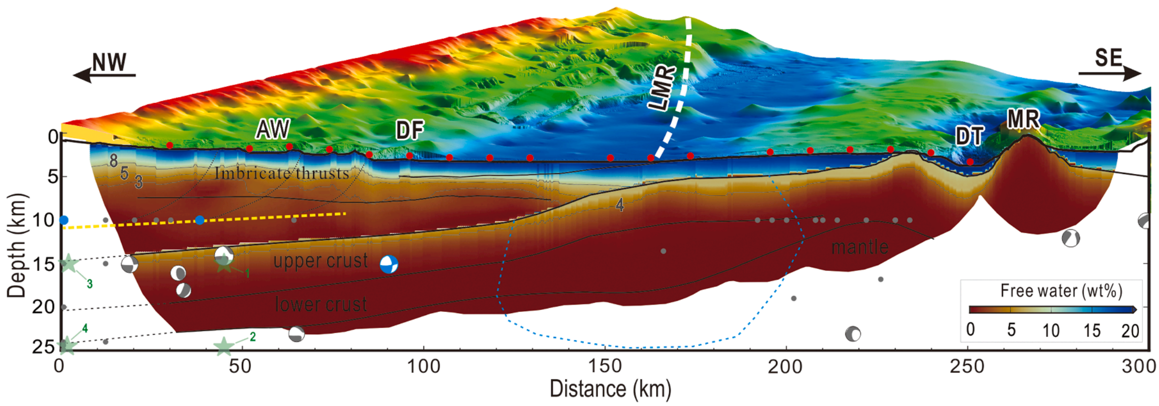

Fig. 8. A schematic model illustrating the structure, seismicity, and water content of MSZ based on the velocity model. Black lines denote the interfaces of the oceanic subducting slab, including the sedimentary unconformity, basement, upper-lower crustal interface, and Moho discontinuity. The yellow dashed line and the sloping black dotted line above it represent the décollement and imbricate thrust faults, respectively, based on the results of Kopp et al. (2000) and Smith et al. (2012). The orange dashed curve corresponds to the low-density underplating zone below the LMR in Fig. 8. Blue circles and blue-white focal solution depict historical seismic events immediately adjacent to the section from the USGS and the Global Centroid Moment Tensor (GCMT), respectively. Gray circles (USGS) and gray-white focal solutions (GCMT) represent historical seismic activities at the same latitude within 100 km near the profile. The four translucent green stars represent the possible focal locations of the 1945 earthquake: 1 (NGDC), 2 (Heidarzadeh et al., 2008; Smith et al., 2012), 3 (USGS), 4 (Byrne et al., 1992; Pararas-Carayannis et al., 2006).

by strike-slip extension between the Arabian and Indian plates near the Dalrymple Trough. Further analysis is necessary to determine the exact nature of these differences and their implications on the north and south areas of the LMR.

4.3. Upper crust hydration

The upper crustal velocities of the subducted slab in the MSZ exhibit lower values compared to typical oceanic crust in the Pacific and Atlantic oceans, but they are similar to or slightly lower than those observed in other Indian Ocean regions (Fig. 7a-c). Conversely, the lower crustal velocity structure resembles that of oceanic crust and is significantly higher than the continental crust (Fig. 7d). This atypical velocity reduction in the upper crust is interpreted as indicative of a substantial water content. Many studies on the water content of subducted plates (e.g., Contreras-Reyes et al., 2011; Grevemeyer et al., 2007; Ivandic et al., 2008) have demonstrated the development of bending-related faults at the outer rise, providing pathways for water infiltration into the crust. This infiltration gradually reduces the crustal velocity of subducting plates from outer rise to the trench. This phenomenon is also observed in typical low-angle subduction zone areas, such as the Sunda and Chile subduction zone (Shulgin et al., 2011; Grevemeyer et al., 2018). However, in the MSZ, the crustal velocity does not exhibit a gradual decrease towards the deformation front, as observed in most subduction zones. We propose that this is due to the presence of thick impermeable sedimentary cover in the MSZ, which blocks direct contact between the fault activated in the outer rise region and the water. Consequently, fluid circulation within the subduction plate is shut off, resulting in no velocity reduction from the outer rise to the deformation front. Conversely, with the rapid thickening of accretionary wedge deposits, preexisting bending-related faults of subducted plates may be partially healed under considerable load and high temperature conditions. Laboratory measurements indicate that crusstal velocity increases by 0.37–0.40 km/s due to the closure of microcracks under the pressure of approximately 4 km thick sediments, which is consistent with the statistical results of the global oceanic crust that thick sediments may increase the underlying crust velocity by collapsing lava tubes and fractures (Christeson et al., 2019).

In addition, compared to subducting oceanic crust affected by hydration, the crustal velocities in Makran (gray envelope in Fig. 7h) are slightly higher than those of high-angle subduction zones such as South Mariana and slightly lower than those of low-angle subduction zones such as Sunda, Cascadia, Middle America and Chile, indicating a moderate water content in the upper crust of Makran. Crustal porosity distribution characteristics are determined through empirical relationships of crustal V_p-porosity (see Text S1), and the free water content of the crust is estimated (Fig. 8, Text S3). The results reveal that crustal porosity can exceed 10%, with corresponding water content exceeding 4.0 wt% in the shallow 1–2 km depth of the upper crust. This content is slightly higher than in other subduction zones such as the Middle America (Ivandic et al., 2008), Cascadia (Canales et al., 2017), Alaska and Sumatra (Acquisto et al., 2022). However, the unusually high-water content in the upper crust of Makran differs from that in other subduction zones, where water enters the crust through bending-related faults in the outer rise region. It may originate from water stored in the pre-existing oceanic fabric during crust formation or subsequent tectonic events, becoming trapped in the crust under rapid burial by low-permeability sediments. Controlled source electromagnetic studies have indicated that the porosity of the shallow part of the upper crust in the Middle America subduction plate can reach 2.7–12% before bending (Naif et al., 2015), suggesting that the crust may contain considerable water before hydration in the outer rise region. Increased temperatures and high pressures resulting from thick sedimentary cover may prevent the expansion of crustal fluid, leading to overpressure fluids at the interface between the igneous crust and sediments. The widespread presence of mud volcanoes in the accretion wedge of Makran also indicates deep high-pressure fluids. The water content of the subducted upper crust surpasses that of the subducted sediments, as illustrated in Fig. 8. Consequently, the *Vp*-derived free water content suggests that the input water of the incoming plate in MSZ is predominantly stored in the upper crust, while the subducted sediments and lower crust remain comparatively dry.

4.4. Seismotectonic implications

In the vicinity of the survey profile in the Makran region, few seismic events of magnitude less than M_w 4.0 have been recorded due to the scarcity of a comprehensive local seismological network. The mechanical strength and megathrust slip behavior in subduction zones, particularly those covered by thick sediments, are significantly influenced by the consolidation state of subducted sediments, which can contribute to the development of large earthquake ruptures (Han et al., 2017). The sediments in the MSZ have been significantly strengthened through mechanical compaction and diagenesis prior to subduction, akin to observations in other subduction zones such as Cascadia (Han et al., 2017) and Sumatra (Dean et al.,2010; Hüpers et al., 2017), where subducted consolidated sediments are thought to develop large earthquake ruptures. Smith et al. (2012) propose that the consolidation state of high-V_p sediments at décollement depth in Makran is sufficient to support earthquake rupture. Several seismic events with a magnitude greater than M_w 4.0 have been observed near the depth of the décollement, as depicted in Fig. 8. The mean shear stress and effective friction coefficient results of the megathrust, calculated by Penney et al. (2017), indicate that the MSZ is similar to non-sediments subduction zones. Consolidated sediments possess sufficient mechanical strength to support considerable strain accumulation and efficient elastic stress transfer during earthquake rupture (Hüpers et al., 2017; Han et al., 2017). Moreover, increased temperatures induced by the thick sedimentary coverage in Makran, with décollement temperatures near the deformation front corresponding to the 150 °C isotherm (Smith et al., 2013; Khaledzadeh and Ghods, 2022), extend the seismogenic zone to shallow depths and promotes long-distance megathrust rupture (Han et al., 2017). As a result, the décollement in the MSZ may potentially develop large thrust earthquakes. The scarcity of recorded seismic events may be attributed to limited local station records and long seismic intervals characteristic of this subduction zone.

While seismicity in Makran may not be extensively documented, Fig. 8 illustrates its occurrence along all structural interfaces of the subducting plate. In particular, the high-water content in the shallow crust and the low permeability compacted sedimentary cover lead to overpressured pore water at the basement interface. This overpressured fluid can significantly affect earthquake rupture mechanism through modulation of seismic coupling and regulation of effective stress, as reported by Frohling and Szeliga (2016) and Acquisto et al. (2022). Canales et al. (2017) propose that the accumulation of overpressured fluid in the upper crust of the subducting plate in Cascadia can facilitate episodic tremor and slip events, as well as low-frequency earthquakes. In the MSZ, several medium-magnitude earthquakes have occurred in the vicinity of the uppermost crust, where there is a slight concentration of water near the basement interface (Fig. 8). According to the NGDC earthquake catalog, the 1945 earthquake was estimated to have occurred near the model distance of 45 km, with a source depth of 15 km (Fig. 8). However, Heidarzadeh et al. (2008) and Smith et al. (2012) suggested a focal depth range of 25–30 km for the earthquake. Conversely, based on the USGS earthquake catalog, the earthquakes occurred near the same latitude as the model distance of 0 km, with a focal depth of 15 km. Byrne et al. (1992) and Pararas-Carayannis et al. (2006) provided earthquake location information indicating a focal depth range of 25–27 km.

Our model indicates that the shallow subduction angle (~2°) results in little depth change of the plate interface landward and minimal variations in deep structure along the direction parallel to the deformation front, as reported by Kopp et al. (2000). The focal depth of the 1945 earthquake, whether occurred near the deformation front (according to the NGDC catalog) or at the latitude of the model distance of 0 km (as the USGS catalog), suggests that a depth of 25 km (e.g., Byrne et al., 1992) would likely place the earthquake origin at the Moho discontinuity or the upper mantle top region, based on our velocity model. Conversely, a focal depth of 15 km indicates a slip earthquake of the basement interface rather than the décollement inside the accretion wedge. Yang et al. (2022) proposed that the 2017 Pasni earthquake (M_w 6.3) was the largest offshore event after the 1945 earthquake, with a focal depth of 13–14 km, near the basement rather than the décollement or the deeper interface (e.g., 29 km given by USGS). Our modeling results and the previously reported focal depths indicate that the 1945 earthquake was likely a slip earthquake that occurred near the basement or the Moho interface rather than the décollement in the accretion wedge. The high-water content of the uppermost crust near the basement may change the coupling state between the igneous crust and the consolidated subducting sediments with increasing subduction plate temperature, thus promoting slip fracture on the interface. We suggest that the basement is more likely to experience slip fracture than the Moho interface. As multiple interfaces may slip off in the MSZ during plate subduction, further investigations are required to assess their possible location and seismogenic mechanisms.

5. Conclusions

This study presents a high-resolution velocity model of the Makran Subduction Zone obtained through a wide-angle ocean bottom seismometer experiment from Dalrymple Trough to the coastal area of Pakistan. We identify a well-constrained crust with a thickness ranging from 6 to 12 km and a plate subduction dip of ~2° The observed atypical crustal structure may be related to magmatic activity and the hydration process of subducted plates.

Our findings reveal that the accretion wedge thickness exceeds 13 km, and the incoming sediments reaching up to 8.5 km in thickness. Significantly, we observe an abrupt change in porosity gradient at a depth of ~4.5 km, suggesting significant dewatering and compaction of the incoming sediments prior to subduction. Below this interface depth, the sediments have minor variations in mechanical properties during subduction.

Moreover, our model highlights significant differences in crustal structure between the north and south sides of the LMR, potentially indicating different tectonic sources or processes. The LMR may represent a paleo-ocean boundary, with the possibility of low-density underplating beneath it.

Our findings also suggest that the input free water of the incoming plate in MSZ is mainly stored in the uppermost crust, resulting in the presence of overpressured fluid at the basement interface that could significantly influence earthquake rupture mechanisms. Seismic activity occurs along all structural interfaces, including the décollement, basement, upper-lower crustal interface, and Moho discontinuity, indicating the potential for multiple interfaces to experience slip during subduction. Both the décollement and basement interface are identified as potential triggers for large earthquakes in the MSZ.

CRediT authorship contribution statement

Chuanhai Yu: Writing – original draft, Visualization, Methodology, Investigation, Funding acquisition. **Min Xu:** Writing – review & editing, Supervision, Funding acquisition, Formal analysis, Conceptualization. **Jian Lin:** Writing – review & editing, Validation, Resources, Investigation, Funding acquisition, Conceptualization. **Hongfeng Yang:** Writing – review & editing, Investigation. **Xu Zhao:** Writing – review & editing, Visualization, Methodology, Investigation. **Xin Zeng:** Writing – review & editing, Investigation, Data curation. **Enyuan He:** Writing – review & editing, Visualization, Methodology. **Fan Zhang:** Writing – review & editing, Investigation. **Zhen Sun:** Writing – review & editing, Investigation.

Declaration of competing interest

The authors declare that they have no known competing financial interests or personal relationships that could have appeared to influence the work reported in this paper.

Data availability

The final velocity model and all the raw seismic data used in this study can be visited through the link (https://doi.org/10.57760/sciencedb.07891). The earthquake catalog data are from the USGS (https://www.earthquake.usgs.gov/earthquakes/search/), the NGDC (https://www.ngdc.noaa.gov/hazel/view/hazards/earthquake/search), and the GCMT (https://www.globalcmt.org/), respectively.

Acknowledgments

We thank the captain, crew, scientists, and technical staff of R/V ShiYan 3 during the China-Pakistan First Joint Expedition of the Makran Trench. We also benefited from the discussion with the Marine Seismology and Deep Ocean Geodynamic Groups at the SCSIO. We greatly appreciate the efforts of the editor Hans Thybo, the reviewer Dr. Alexey Shulgin, and an anonymous reviewer for their insightful comments, suggestions, and constructive criticism. This work was supported by the National Natural Science Foundation of China (42306087), the Guangdong Basic and Applied Basic Research Foundation (2021B1515020023; 2022A1515110879), and the Chinese Academy of Sciences (Y4SL021001, 133244KYSB20180029, 131551KYSB20200021, and ISEE2021PY03). Some figures were drafted using Generic Mapping Tools (https://www.generic-mapping-tools.org).

Supplementary materials

Supplementary material associated with this article can be found, in the online version, at doi:10.1016/j.epsl.2024.118896.

References

Acquisto, T., Bécel, A., Singh, S.C., Carton, H., 2022. Evidence of strong upper oceanic crustal hydration outboard the Alaskan and Sumatran subduction zones. J. Geophys. Res., Solid Earth 127 (10), e2022JB024751. https://doi.org/10.1029/2022JB024751.

Allen, R.W., Collier, J.S., Henstock, T.J., The VoiLA Consortium, 2022. The role of crustal accretion variations in determining slab hydration at an Atlantic subduction zone. J. Geophys. Res., Solid Earth 127 (8), e2022JB024349. https://doi.org/10.1029/2022JB024349.

Altenbernd, T., Jokat, W., Geissler, W., 2020. The bent prolongation of the 85° E Ridge south of 5° N–Fact or fiction? Tectonophysics 785, 228457. https://doi.org/10.1016/j.tecto.2020.228457.

Altenbernd, T., Jokat, W., Geissler, W., Haberland, C., De Silva, N., 2022. Wide-angle seismic transect reveals the crustal structure of (f) southern Sri Lanka. Tectonophysics 833, 229358. https://doi.org/10.1016/j.tecto.2022.229358.

Barton, P.J., Owen, T.R.E., White, R.S., 1990. The deep structure of the east Oman continental margin: preliminary results and interpretation. Tectonophysics 173 (1–4), 319–331. https://doi.org/10.1016/0040-1951(90)90227-Y.

Bletery, Q., Thomas, A.M., Rempel, A.W., Karlstrom, L., Sladen, A., De Barros, L., 2016. Mega-earthquakes rupture flat megathrusts. Science 354 (6315), 1027–1031. https://doi.org/10.1126/science.aag048.

Byrne, D.E., Sykes, L.R., Davis, D.M., 1992. Great thrust earthquakes and aseismic slip along the plate boundary of the Makran subduction zone. J. Geophys. Res., Solid Earth 97 (B1), 449–478. https://doi.org/10.1029/91JB02165.

Canales, J.P., Carbotte, S.M., Nedimović, M.R., Carton, H., 2017. Dry Juan de Fuca slab revealed by quantification of water entering Cascadia subduction zone. Nature Geosci 10 (11), 864–870. https://doi.org/10.1038/NGEO3050.

Christeson, G.L., Goff, J.A., Reece, R.S., 2019. Synthesis of oceanic crustal structure from two-dimensional seismic profiles. Rev. Geophys. 57 (2), 504–529. https://doi.org/10.1029/2019RG000641.

Christensen, N.I., Mooney, W.D., 1995. Seismic velocity structure and composition of the continental crust: a global view. J. Geophys. Res., Solid Earth 100 (B6), 9761–9788. https://doi.org/10.1029/95JB00259.

Contreras-Reyes, E., Grevemeyer, I., Flueh, E.R., Reichert, C., 2008. Upper lithospheric structure of the subduction zone offshore of southern Arauco peninsula, Chile, at ~38 S. J. Geophys. Res., Solid Earth 113 (B7). https://doi.org/10.1029/2007JB005569.

Contreras-Reyes, E., Grevemeyer, I., Watts, A.B., Planert, L., Flueh, E.R., Peirce, C., 2010. Crustal intrusion beneath the Louisville hotspot track. Earth Planet. Sci. Lett. 289 (3–4), 323–333. https://doi.org/10.1016/j.epsl.2009.11.020.

Contreras-Reyes, E., Grevemeyer, I., Watts, A.B., Flueh, E.R., Peirce, C., Moeller, S., Papenberg, C., 2011. Deep seismic structure of the Tonga subduction zone: implications for mantle hydration, tectonic erosion, and arc magmatism. J. Geophys. Res., Solid Earth 116 (B10). https://doi.org/10.1029/2011JB008434.

Contreras-Reyes, E., Obando-Orrego, S., Cortés-Rivas, V., Krabbenhoeft, A., 2022. Poisson's ratio structure beneath the Nazca Ridge. Geophys. Res. Lett. 49 (9), e2021GL097018 https://doi.org/10.1029/2021GL097018.

Contreras-Reyes, E., Obando-Orrego, S., Grevemeyer, I., 2023. 2-D Vp and Vs models of the Indian oceanic crust adjacent to the NinetyEast Ridge. J. Geophys. Res., Solid Earth, e2022JB025701. https://doi.org/10.1029/2022JB025701.

Dean, S.M., McNeill, L.C., Henstock, T.J., Bull, J.M., Gulick, S.P., Austin Jr, J.A., Bangs, N.L., Djajadihardja, Y.S., Permana, H., 2010. Contrasting décollement and prism properties over the Sumatra 2004–2005 earthquake rupture boundary. Science 329 (5988), 207–210. https://doi.org/10.1126/science.1189373.

Edwards, R.A., Minshull, T.A., Flueh, E.R., Kopp, C., 2008. Dalrymple Trough: an active oblique-slip ocean-continent boundary in the northwest Indian Ocean. Earth Planet. Sci. Lett. 272 (1–2), 437–445. https://doi.org/10.1016/j.epsl.2008.05.007.

Edwards, R.A., Minshull, T.A., White, R.S., 2000. Extension across the Indian–Arabian plate boundary: the Murray Ridge. Geophys. J. Int. 142 (2), 461–477. https://doi.org/10.1046/j.1365-246x.2000.00163.x.

Fowler, S.R., White, R.S., Louden, K.E., 1985. Sediment dewatering in the Makran accretionary prism. Earth Planet. Sci. Lett. 75 (4), 427–438. https://doi.org/10.1016/0012-821X(85)90186-4.

Frohling, E., Szeliga, W., 2016. GPS constraints on interplate locking within the Makran subduction zone. Geophys. J. Int. 205 (1), 67–76. https://doi.org/10.1093/gji/ggw001.

Grando, G., McClay, K., 2007. Morphotectonics domains and structural styles in the Makran accretionary prism, offshore Iran. Sedimentary Geol 196 (1–4), 157–179. https://doi.org/10.1016/j.sedgeo.2006.05.030.

Grevemeyer, I., Flueh, E.R., Reichert, C., Bialas, J., Kläschen, D., Kopp, C., 2001. Crustal architecture and deep structure of the Ninetyeast Ridge hotspot trail from active-source ocean bottom seismology. Geophys. J. Int. 144 (2), 414–431. https://doi.org/10.1046/j.0956-540X.2000.01334.x.

Grevemeyer, I., Ranero, C.R., Flueh, E.R., Kläschen, D., Bialas, J., 2007. Passive and active seismological study of bending-related faulting and mantle serpentinization at the Middle America trench. Earth Planet. Sci. Lett. 258 (3–4), 528–542. https://doi.org/10.1016/j.epsl.2007.04.013.

Grevemeyer, I., Ranero, C.R., Ivandic, M., 2018. Structure of oceanic crust and serpentinization at subduction trenches. Geosphere 14 (2), 395–418. https://doi.org/10.1130/GES01537.1.

Haberland, C., Mokhtari, M., Babaei, H.A., Ryberg, T., Masoodi, M., Partabian, A., Lauterjung, J., 2020. Anatomy of a crustal-scale accretionary complex: insights from deep seismic sounding of the onshore western Makran subduction zone. Iran. Geol. 49 (1), 3–7. https://doi.org/10.1130/G47700.1.

Han, S., Bangs, N.L., Carbotte, S.M., Saffer, D.M., Gibson, J.C., 2017. Links between sediment consolidation and Cascadia megathrust slip behaviour. Nat. Geosci. 10 (12), 954–959. https://doi.org/10.1038/s41561-017-0007-2.

He, E., Qiu, X., Chen, C., Wang, Y., Xu, M., Zhao, M., You, Q., 2023. Deep crustal structure across the Challenger Deep: tectonic deformation and strongly serpentinized layer. Gondwana Res. https://doi.org/10.1016/j.gr.2023.02.020.

Heidarzadeh, M., Pirooz, M.D., Zaker, N.H., Yalciner, A.C., Mokhtari, M., Esmaeily, A., 2008. Historical tsunami in the Makran Subduction Zone off the southern coasts of Iran and Pakistan and results of numerical modeling. Ocean Eng. 35 (8–9), 774–786. https://doi.org/10.1016/j.oceaneng.2008.01.017.

Hutchison, I., Louden, K.E., White, R.S., Von Herzen, R.P., 1981. Heat flow and age of the Gulf of Oman. Earth Planet. Sci. Lett. 56, 252–262. https://doi.org/10.1016/0012-821X(81)90132-1.

Hüpers, A., Torres, M.E., Owari, S., McNeill, L.C., Dugan, B., Henstock, T.J., Milliken, K. L., Petronotis, K.E., Backman, J., Bourlange, S., Chemale, F., Chen, W., Colson, T.A., Frederik, M.C.G., Guèrin, G., Hamahashi, M., House, B.M., Jeppson, T.N., Kachovich, S., Kenigsberg, A.R., Kuranaga, M., Kutterolf, S., Mitchison, F.L., Mukoyoshi, H., Nair, N., Pickering, K.T., Pouderoux, H.F.A., Shan, Y., Song, I., Vannucchi, P., Vrolijk, P.J., Yang, T., Zhao, X., 2017. Release of mineral-bound water prior to subduction tied to shallow seismogenic slip off Sumatra. Science 356 (6340), 841–844. https://doi.org/10.1126/science.aal3429.

Ivandic, M., Grevemeyer, I., Berhorst, A., Flueh, E.R., McIntosh, K., 2008. Impact of bending related faulting on the seismic properties of the incoming oceanic plate offshore of Nicaragua. J. Geophys. Res., Solid Earth 113 (B5). https://doi.org/10.1029/2007JB005291.

Khaksar, A., Griffiths, C., 2000. Effects of porosity and clay content on P-and S-wave velocities in cooper basin sandstones. Explor. Geophys. 31 (2), 433–440. https://doi.org/10.1071/EG00433.

Khaledzadeh, M., Ghods, A., 2022. Estimation of size of megathrust zone in the Makran subduction system by thermal modelling. Geophys. J. Int. 228 (3), 1530–1540. https://doi.org/10.1093/gji/ggab417.

Kopp, C., Fruehn, J., Flueh, E.R., Reichert, C., Kukowski, N., Bialas, J., Klaeschen, D., 2000. Structure of the Makran subduction zone from wide-angle and reflection seismic data. Tectonophysics 329 (1–4), 171–191. https://doi.org/10.1016/S0040-1951(00)00195-5.

Korenaga, J., Holbrook, W.S., Kent, G.M., Kelemen, P.B., Detrick, R.S., Larsen, H.C., Hopper, J.R., Dahl-Jensen, T., 2000. Crustal structure of the southeast Greenland margin from joint refraction and reflection seismic tomography. J. Geophys. Res., Solid Earth 105 (B9), 21591–21614. https://doi.org/10.1029/2000JB900188.

Kukowski, N., Schillhorn, T., Flueh, E.R., Huhn, K., 2000. Newly identified strike-slip plate boundary in the northeastern Arabian Sea. Geology 28 (4), 355–358. https://doi.org/10.1130/0091-7613(2000)28<355:NISPBI>2.0.CO;2.

Lin, Y.N., Jolivet, R., Simons, M., Agram, P.S., Martens, H.R., Li, Z., Lodi, S.H., 2015. High interseismic coupling in the Eastern Makran (Pakistan) subduction zone. Earth Planet. Sci. Lett. 420, 116–126. https://doi.org/10.1016/j.epsl.2015.03.037.

Lv, X., Amelung, F., Shao, Y., 2022. Widespread aseismic slip along the Makran megathrust triggered by the 2013 M_w 7.7 Balochistan earthquake. Geophys. Res. Lett. 49 (6), e2021GL097411 https://doi.org/10.1029/2021GL097411.

Meyer, B., Chulliat, A., Saltus, R., 2017. Derivation and error analysis of the earth magnetic anomaly grid at 2 resolution version 3 (EMAG2v3). Geochem. Geophys. Geosyst. 18 (12), 4522–4537. https://doi.org/10.1002/2017GC007280.

Minshull, T.A., Edwards, R.A., Flueh, E.R., 2015. Crustal structure of the Murray Ridge, northwest Indian Ocean, from wide-angle seismic data. Geophys. J. Int. 202 (1), 454–463. https://doi.org/10.1093/gji/ggv162.

Minshull, T.A., Lane, C.I., Whitmarsh, R.B., 2008. The relationship between rifting and magmatism in the northeastern Arabian Sea. Nat. Geosci. 1 (7), 463–467. https://doi.org/10.1038/ngeo228.

Minshull, T., White, R., 1989. Sediment compaction and fluid migration in the Makran accretionary prism. J. Geophys. Res., Solid Earth 94 (B6), 7387–7402. https://doi.org/10.1029/JB094iB06p07387.

Motaghi, K., Shabanian, E., Nozad-Khalil, T., 2020. Deep structure of the western coast of the Makran subduction zone, SE Iran. Tectonophysics 776, 228314. https://doi.org/10.1016/j.tecto.2019.228314.

Naif, S., Key, K., Constable, S., Evans, R.L., 2015. Water-rich bending faults at the Middle America Trench. Geochem. Geophys. Geosyst. 16 (8), 2582–2597. https://doi.org/10.1002/2015GC005927.

Niu, X., Ruan, A., Li, J., Minshull, T.A., Sauter, D., Wu, Z., Qiu, X., Zhao, M., Chen, Y.J., Singh, S., 2015. Along-axis variation in crustal thickness at the ultraslow spreading Southwest Indian Ridge (50° E) from a wide-angle seismic experiment. Geochem. Geophys. Geosyst. 16 (2), 468–485. https://doi.org/10.1002/2014GC005645.

Olsen, K.M., Bangs, N.L., Tréhu, A.M., Han, S., Arnulf, A., Contreras-Reyes, E., 2020. Thick, strong sediment subduction along south-central Chile and its role in great earthquakes. Earth planet. Sci. Lett. 538, 116195 https://doi.org/10.1016/j.epsl.2020.116195.

Pajang, S., Cubas, N., Letouzey, J., Le Pourhiet, L., Seyedali, S., Fournier, M., Agard, P., Mahdi Khatib, M., Heyhat, M., Mokhtari, M., 2021. Seismic hazard of the western Makran subduction zone: insight from mechanical modelling and inferred frictional properties. Earth planet. Sci. Lett. 562, 116789 https://doi.org/10.1016/j.epsl.2021.116789.

Pararas-Carayannis, G., 2006. The potential of tsunami generation along the Makran Subduction Zone in the northern Arabian Sea: case study: the earthquake and tsunami of November 28, 1945. Sci. Tsunami Hazards 24 (5), 358–384.

Parvaiz, S., Ali, A., Javed, F., Shah, M.A., 2022. Deformational pattern and seismogenic potential of the eastern Makran subduction zone. J. Asian Earth Sci. 235, 105298 https://doi.org/10.1016/j.jseaes.2022.105298.

Penney, C., Tavakoli, F., Saadat, A., Nankali, H.R., Sedighi, M., Khorrami, F., Sobouti, F., Rafi, Z., Copley, A., Jackson, J., 2017. Megathrust and accretionary wedge properties and behaviour in the Makran subduction zone. Geophys. J. Int. 209, 1800–1830. https://doi.org/10.1093/gji/ggx126.

Planert, L., Kopp, H., Lueschen, E., Mueller, C., Flueh, E.R., Shulgin, A., Djajadihardja, Y., Krabbenhöft, A., 2010. Lower plate structure and upper plate deformational segmentation at the Sunda-Banda arc transition, Indonesia. J. Geophys. Res., Solid Earth 115 (B8). https://doi.org/10.1029/2009JB006713.

Priestley, K., Sobouti, F., Mokhtarzadeh, R., A Irandoust, M., Ghods, R., Motaghi, K., Ho, T., 2022. New constraints for the on-shore Makran Subduction Zone crustal structure. J. Geophys. Res., Solid Earth 127 (1), e2021JB022942. https://doi.org/10.1029/2021JB022942.

Rodriguez, M., Huchon, P., Chamot-Rooke, N., Fournier, M., Delescluse, M., Smit, J., Plunder, A., Calvès, G., Ninkabou, D., Pubellier, M., François, T., Agard, P., Gorini, C., 2020. Successive shifts of the India-Africa transform plate boundary during the Late Cretaceous-Paleogene interval: implications for ophiolite emplacement along transforms. J. Asian Earth Sci. 191, 104225 https://doi.org/10.1016/j.jseaes.2019.104225.

Sandwell, D.T., Müller, R.D., Smith, W.H., Garcia, E., Francis, R., 2014. New global marine gravity model from CryoSat-2 and Jason-1 reveals buried tectonic structure. Science 346 (6205), 65–67. https://doi.org/10.1126/science.1258213.

Scholl, D.W., Kirby, S.H., von Huene, R., Ryan, H., Wells, R.E., Geist, E.L., 2015. Great (≥ M_w8. 0) megathrust earthquakes and the subduction of excess sediment and bathymetrically smooth seafloor. Geosphere 11 (2), 236–265. https://doi.org/10.1130/GES01079.1.

Shulgin, A., Kopp, H., Klaeschen, D., Papenberg, C., Tilmann, F., Flueh, E.R., Franke, D., Barckhausen, U., Krabbenhoeft, A., Djajadihardja, Y., 2013. Subduction system variability across the segment boundary of the 2004/2005 Sumatra megathrust earthquakes. Earth Planet. Sci. Lett. 365, 108–119. https://doi.org/10.1016/j.epsl.2012.12.032.

Shulgin, A., Kopp, H., Mueller, C., Planert, L., Lueschen, E., Flueh, E.R., Djajadihardja, Y., 2011. Structural architecture of oceanic plateau subduction offshore Eastern Java and the potential implications for geohazards. Geophys. J. Int. 184 (1), 12–28. https://doi.org/10.1111/j.1365-246X.2010.04834.x.

Smith, G.L., McNeill, L.C., Henstock, T.J., Arraiz, D., Spiess, V., 2014. Fluid generation and distribution in the highest sediment input accretionary margin, the Makran. Earth Planet. Sci. Lett. 403, 131–143. https://doi.org/10.1016/j.epsl.2014.06.030.

Smith, G., McNeill, L., Henstock, T.J., Bull, J., 2012. The structure and fault activity of the Makran accretionary prism. J. Geophys. Res., Solid Earth 117 (B7). https://doi.org/10.1029/2012JB009312.

Smith, G.L., McNeill, L.C., Wang, K., He, J., Henstock, T.J., 2013. Thermal structure and megathrust seismogenic potential of the Makran subduction zone. Geophys. Res. Lett. 40 (8), 1528–1533. https://doi.org/10.1002/grl.50374.

Teknik, V., Ghods, A., Thybo, H., Artemieva, I.M., 2019. Crustal density structure of the northwestern Iranian Plateau. Can. J. Earth Sci. 56 (12), 1347–1365. https://doi.org/10.1139/cjes-2018-0232.

Van Avendonk, H.J., Holbrook, W.S., Lizarralde, D., Denyer, P., 2011. Structure and serpentinization of the subducting Cocos plate offshore Nicaragua and Costa Rica. Geochem. Geophys. Geosyst. 12 (6) https://doi.org/10.1029/2011GC003592.

Velde, B., 1996. Compaction trends of clay-rich deep sea sediments. Mar. Geol. 133 (3–4), 193–201. https://doi.org/10.1016/0025-3227(96)00020-5.

Watts, A.B., Grevemeyer, I., Shillington, D.J., Dunn, R.A., Boston, B., Gómez de La Peña, L., 2021. Seismic structure, gravity anomalies and flexure along the Emperor Seamount chain. J. Geophys. Res., Solid Earth 126 (3), e2020JB021109. https://doi.org/10.1029/2020JB021109.

White, R.S., Klitgord, K., 1976. Sediment deformation and plate tectonics in the Gulf of Oman. Earth Planet. Sci. Lett. 32 (2), 199–209. https://doi.org/10.1016/0012-821X(76)90059-5.

White, R.S., McKenzie, D., O'Nions, R.K., 1992. Oceanic crustal thickness from seismic measurements and rare earth element inversions. J. Geophys. Res., Solid Earth 97 (B13), 19683–19715. https://doi.org/10.1029/92JB01749.

Whitmarsh, R.B., 1979. The Owen Basin off the south-east margin of Arabia and the evolution of the Owen Fracture Zone. Geophys. J. Int. 58 (2), 441–470. https://doi.org/10.1111/j.1365-246X.1979.tb01034.x.

Yang, X., Qiu, Q., Feng, W., Lin, J., Zhang, J., Zhou, Z., Zhang, F., 2022. Mechanism of the 2017 M_w 6.3 Pasni earthquake and its significance for future major earthquakes in the eastern Makran. Geophys. J. Int. 231 (2), 1434–1445. https://doi.org/10.1093/gji/ggac257.

Zhao, M., Qiu, X., Li, J., Sauter, D., Ruan, A., Chen, J., Cannat, M., Singh, S., Zhang, J., Wu, Z., Niu, X., 2013. Three-dimensional seismic structure of the Dragon Flag oceanic core complex at the ultraslow spreading Southwest Indian Ridge (49°39′E). Geochem. Geophys. Geosyst. 14 (10), 4544–4563. https://doi.org/10.1002/ggge.20264.